Experiment and RANS modeling of solitary wave impact on a vertical wall mounted on a reef flat

Kezhao Fang[a,*], Li Xiao[a], Zhongbo Liu[b*], Jiawen Sun[c], Ping Dong[d], Hao Wu[a]

(a *State Key Laboratory of Coastal and Offshore Engineering, Dalian University of Technology Dalian, 116024, China;* b *Transportation Engineering College, Dalian Maritime University, Dalian, 116024, China;* c *National Marine Environmental Monitoring Center, Dalian, 116024, China;* d *Civil Engineering and Industrial Design, University of Liverpool, UK*)

Corresponding author' email: kfang@dlut.edu.cn

Abstract: A series of two-dimensional flume experiments were carried out to study turbulent bore impact on the vertical wall mounted on a reef flat. Turbulent bores were generated by solitary waves propagating on typical fringing reef profiles with and without reef crest. The idealized reef model has a 1:4 face slope and a long reef flat, with an impermeable vertical wall at the end. The solitary wave height varies from 14.1% to 30.0% of the water depth to cover a range of nonlinear wave conditions. Datasets of free surface elevation and flow velocity along fringing reef profiles and pressure on the vertical wall are acquired. Corresponding RANS (Reynolds-averaged Navier–Stokes)-type simulations are performed utilizing the open-source CFD (Computational Fluid Dynamics) OpenFOAM (Open Field Operation and Manipulation) package with the SST k-ω turbulence closure solver and validated using experimental data. The characteristics of the main hydrodynamic and impact processes are examined in detail. The predictive capability of OpenFOAM and three existing formulas for calculating the maximum lateral force are evaluated using measured data. A new predictive equation for peak pressure along the vertical wall is also proposed to achieve better agreement with the experimental data.

Keywords: Solitary wave; fringing reef; OpenFOAM; turbulent bore; pressure; force.

1. Introduction

A typical fringing reef is characterized by a sloping reef face (or a composite of sloping reef faces) with an abrupt transition to an inshore shallow reef platform extending toward the shoreline. Due to the shallow water depth on the reef flat, most of the incident wave energy is dissipated by wave breaking near the reef edge and further weakened while passing through the reef flat due to the large bottom roughness (Nwogu and Demirbilek, 2010; Ma et al., 2014). For this reason, fringing

1

reefs are believed to be able to shelter low-lying coastal areas against hazards such as wave runup, overtopping and erosion (Lowe et al., 2005; Gelfenbaum et al., 2011; Ferrario et al., 2014; Yao et al., 2018; Ning et al., 2019). However, wave-driven coastal hazards still occur in areas fronted by coral reefs during extreme events such as tropical typhoons (Hoeke et al., 2013). Recent studies found that the shelter capability of fringing reefs will be significantly impacted by more frequent and disruptive high-wave events due to the increase in the frequency and intensity of tropical cyclones, as well as sea-level rise in the future (Quataert et al., 2015; Ford and Kench, 2016; Zhang et al., 2017; Storlazzi et al., 2018; Shao et al., 2019; Zheng et al., 2020). Therefore, studying the propagation and transformation of extreme waves over fringing reefs, their dynamic behavior, and hydrodynamic loads on coastal structures is essential for a better understanding of coastal hydrodynamics and hazard mitigation.

Numerous field observations (Lee and Black, 1978; Roeber and Bricker, 2015; Yao et al., 2018), physical experiments (e.g., Nwogu and Demirbilek, 2010), and numerical simulations (e.g., Roeber and Cheung, 2012; Liu et al., 2019) confirm that the breaking waves near reef face or reef edge reform as turbulent bores on reef flat, propagate onshore and finally impact beach or coastal structures. However, these works mainly focus on wave transformation and related coastal hydrodynamics rather than the dynamic response of structures built in the reef environment. Robertson et al. (2013) first attempted to use a series of incident solitary waves to study the effect of turbulent bores on a vertical wall mounted on a fringing reef (with a 1:12 reef slope) in the laboratory. A design formula for the maximum impact force was proposed. The accuracy was improved over existing formulas that were originally designed for calculating wave loads on structures located on normal coastal beaches with steep/mild slopes. However, the effect of the reef crest on the wave loads exerted on structures was not considered in the experiments.

Regarding numerical simulations, the commonly used Boussinesq model (Fang et al., 2015; Liu et al., 2020; Roeber et al., 2010; Zhou et al., 2016) and non-hydrostatic model (Lashley et al., 2018) are inadequate to model violent wave breaking and the interaction between turbulent bores and structures. The most recent RANS model (Kazolea et al., 2019; Li et al., 2019; Yao et al., 2020), LES (Large Eddy Simulation) model (Yao et al., 2019) and SPH model (Lowe et al., 2019; Wen et al., 2019) are used to simulate wave propagation under reef configurations, achieving good

predictions of wave quantities and detailed flow fields. However, these studies did not examine the capability of CFD-type models in reproducing wave loads on structures.

In contrast, tremendous research efforts have been devoted to investigating the tsunami bore impact on coastal structures located along normal coastal beaches (Arikawa et al., 2005; Chuang et al., 2020; Cuomo et al., 2010; Kihara and Kaida, 2019; Ko and Yeh, 2018). Some empirical formulas have also been proposed to calculate the pressure distribution or wave loads exerted by turbulent bores (Ikeno et al., 2001). However, turbulent bores are broken waves. Wave breaking is a complex phenomenon that is not fully understood, especially in the rollers and splashing regions where high-intensity air bubbles are entrained (Lim et al., 2015). The impact exerted by tsunami bores on structures is thus still an open issue. Whether the empirical formula derived from the research on normal coasts with steep/mild beach slopes is reliable in calculating wave loads in the reef environment is of particular interest.

In light of the aforementioned issues, the present study presents an experimental study of the dynamic pressure on a vertical wall mounted on a fringing reef flat under tsunami-like solitary bore impact. A fringing reef profile with a reef crest is considered in the experiments. Meanwhile, a RANS-type simulation using OpenFOAM is also presented. The main characteristics of wave transformation over reef profiles and turbulent bore impact on the vertical wall are investigated. The applicability of existing empirical formulas and OpenFOAM for calculating wave loads is evaluated. New predictive equations are also proposed to achieve better agreement with the measured data.

2. Physical experiments

2.1 *Wave flume set up*

Fig. 1 shows the layout of the experimental wave flume. The experiments were carried out in a wave flume (69 m long, 2 m wide and 1.8 m deep) located in the State Key Laboratory of Coastal and Offshore Engineering, Dalian University of Technology. The lateral sides of the wave flume are glass sidewalls, which are convenient for camera recording and visual observation of the wave evolution process. Solitary waves were generated by a piston-type wavemaker at one end of the flume using the method proposed by Goring (1978). The water depth was kept constant, equal to 0.493 m, during the experiments.

As shown in Fig. 1, the idealized fringing reef profile is 0.4 m high, with a steep 1:4 front slope connected by a 6 m long reef flat. The surface of the reef slope and reef flat is made of smooth plexiglass, which significantly reduces the bottom friction. A vertical wall with a height of 0.6 m is installed at the end of the reef flat. The reef model is positioned 38.89 m from the wavemaker and firmly supported by steel frames. Silicone fills the borders between the reef model and glass walls to prevent fluid infiltration. An optional reef crest is also made of smooth plexiglass, with a height of 0.083 m and a length of 0.75 m. Both the offshore and onshore sides of the crest have the same slope as the front reef, that is, 1:4. For these two reef configurations, the minimum water depths of the reef flat and reef crest are 0.093 m and 0.01 m, respectively.

2.2 *Measurement apparatus*

The free surface elevation along the flume during experiments was measured using 32 wave gauges, and their locations are sketched in Fig. 1. G4 – G7 were located at the flat part of the flume to monitor the incident and reflected waves. G8 was precisely positioned above the beach toe (x=38.89). G7 – G21 cover the entire reef slope and part of the reef flat with an interval of 0.2 m. G22 – G31 (with an interval of 0.3 m) and G32 cover the rest of the reef flat. G32 is positioned 1.41 m before the vertical wall and was used to obtain the incoming turbulent bore height. Four acoustic doppler velocimetry sensors (ADV1@x=39.81 m, ADV2@x=40.91 m, ADV3@x=42.69 m, ADV4@x=44.04 m) were used to measure the flow velocity. The probe of ADVS is approximately 0.04 m above the reef surface. The second velocity sensor ADV2 was moved to x=42.07 m to avoid interference with the reef crest model once the reef crest was installed onto the topography. Fifteen tiny pressure transducers, each with a diameter of 0.004 m, were fixed flush to the front face of the vertical wall at a spacing of 0.02 m and were placed in a vertical array with the lower sensor located 0.02 m above the bottom of the reef flat. All gauges were calibrated before and after experiments to ensure linearity and stability. The sampling rates of the free surface elevation, flow velocity and pressure load are 50 Hz, 50 Hz and 1000 Hz, respectively.

2.2 *Test cases and repeatability*

Given the constant water depth (h) of 0.493 m and the maximum stroke of the wave paddle, the incident solitary wave height (A) varies from 14.1% to 30% of the water depth to cover a range of nonlinear wave conditions, as listed in Table 1. The corresponding wave height measured at G4 (approximately 10 m offshore from the beach toe) varies from 0.070 to 0.148 m, named Case 10–

Case 1 hereafter. Each case was repeated at least three times to obtain a reliable dataset. The time histories of free surface elevation, flow velocity, and dynamic pressure on the vertical wall from three runs for Case 1 without a reef crest are presented in Fig. 2. The results show that high repeatability was achieved.

3. Numerical model

OpenFOAM is an open-source CFD tool written in a C++ library. It uses the FVM (Finite Volume Method) for spatial discretization and the PISO (Pressure Implicit with Splitting of Operator) algorithm to solve the Navier–Stokes equations for two-phase flows with the VOF (Volume of Fluids) method to capture the fluid interface. OpenFOAM offers many built-in solvers, among which the Waves2Foam solver and the SST k–ω turbulence closure model are adopted in the present simulation. The library waves2Foam is a toolbox used to generate and absorb free surface water waves. The details refer to reference (Jacobsen et al., 2012) and the OpenFOAM website (http://openfoamwiki.net/index.php/Contrib/waves2Foam). This paper focuses on addressing the main issues encountered in the simulation implementation process.

3.1 *Computational domain and boundary conditions*

The ideal numerical wave flume should be the same size as the physical wave flume. However, only the rear part of the physical wave flume was simulated in the actual implementation to save computational costs. The computational domain starts from x=23.89 m to x=46.49 m, and the length is 22.6 m. The following boundary conditions were applied in the simulations: At the inlet, the recorded free surface elevation by G4 and the corresponding velocity components from the shallow water theory of Chappelear (1962) are specified as the target solitary wave signal. The pressure is set to zero normal gradients at all boundaries except the top boundary, where pressure is set to the total pressure. The top boundary is set as the atmosphere. The flume bottom and right end are set as rigid walls with no-slip boundary conditions. The lateral walls are set to empty.

3.2. *Mesh sensitivity validation and numerical settings*

The quadrilateral meshes are used to discretize the computational domain. A series of convergence tests (type 1: Δx=0.002 m, Δz=0.001 m; type 2: Δx=0.005 m, Δz=0.002 m; type 3: Δx=0.01 m, Δz=0.005 m) were conducted to determine the optimal mesh size. Fig. 3 shows the local grid system on the reef face and grid sensitivity testing results. Following Yao et al. (2020), the

maximum free surface elevation (η_{max}) and velocity (u_{max}) obtained by OpenFOAM at the front reef flat in Case 1 without a reef crest (G18, ADV2) are normalized by the incident wave height and $(gh_s)^{0.5}$, respectively (h_s is the water depth at the reef flat) to show convergence. The difference between mesh type 2 and type 1 in terms of wave height and flow velocity is less than 3%, indicating that type 2 can guarantee simulation accuracy. From the reef edge to the back-reef wall, Δx decreases gradually from 0.005 m to 0.004 m to better capture the intense breaking on the reef flat (reef crest) and sudden impact on the vertical wall. Consequently, the total number of meshes is 1968000.

In the following simulations, the density and kinematic viscosity of water are specified as ρ=1000 kg/m³ and v=10⁻⁶ m²/s, while those of air are specified as ρ=1 kg/m³ and v=1.48×10⁻⁵ m²/s. For the turbulence model, a constant turbulent kinetic energy k=10⁻⁶ m²/s² and a specific dissipation rate ω=10⁻⁶ s⁻¹ are specified. The remaining parameters in the turbulence solver use the default values in OpenFOAM. The total simulation time is 17 s, and the Courant number is 0.25 for all cases. The corresponding time step is automatically adjusted during calculations to satisfy stability constraints by both advection and diffusion processes, in which the maximum time step is adequately chosen as 0.001 s. A normalized residual value of order of 1×10⁻⁸ is used to assess simulation convergence. The simulation was run on 16 cores (1 × 80 core Intel(R) Xeon(R) E5-2673 v4@2.30 GHz) of a desktop workstation with 32 GB RAM. The consumed CPU time was approximately 108 hours for each run.

4. Results and discussions

This section presents the computed and experimental results, including free surface elevation, flow velocity, total lateral force and dynamic pressure on the vertical wall. The mean wave dynamics (i.e., TEK and vorticity) from the RANS computation are also presented. Note that both the computed results and measured data are synchronized for comparison, and the moment when the solitary crest reaches x=25.89 m is defined as t=0.

4.1 *General description of mean wave dynamics*

4.1.1 *Fringing reef without crest*

Experimental observations show that solitary waves with different nonlinearities have similar evolutionary patterns over the fringing reef without a crest. The incident wave shoals on the fore slope and breaks as a plunger on the reef flat. The breaking point shifts toward the vertical wall with

decreasing wave amplitude. The plungers then develop into the turbulent bore and impact impulsively upon the vertical wall. Depending on the case, the reflected waves travel offshore in the form of an undular or turbulent bore. Case 1 (A/h=0.3) is chosen here to illustrate the main processes.

Fig. 4 (left) compares the computed and measured wave profiles as the solitary wave propagates across the wave flume. Fig. 5 shows the corresponding mean TKE and vorticity patterns from the RANS simulation. The solitary wave begins to shoal, and the wavefront becomes steep and skews over the fore reef slope due to nonlinear shoaling (t=5.0 s). At approximately t=6.5 s, a plunging breaker formed over the reef flat, characterized by curling crests and almost touching the water ahead. The generated TKE and vorticity are approximately on the order of $O(0.3 \text{ m}^2/\text{s}^2)$ and $O(17 \text{ s}^{-1})$. After this moment, the turbulent bore forms and propagates onshore. The wave profile snapshot at t=7.6 s shows a complicated free surface due to the substantial entrapped air during this process. The locally generated TKE and vorticity at the wavefront are transported downward and backward after the wavefront passes. Finally, the onshore turbulent bore impacts and climbs up the vertical wall (t=8.7 s). The TKE and vorticity intensity decrease at this stage with approximate orders of $O(0.2 \text{ m}^2/\text{s}^2)$ and $O(5 \text{ s}^{-1})$. Compared with the time t=7.6 s, the maximum value of TKE and vorticity dissipated in a large amount but were transported to almost the entire water depth at the rear part of the flume. A blank area with zero TKE and vorticity is found near the reef flat close to the end wall. This area is tightly surrounded by the solid reef bed, end wall and turbulent bore basically on the surface, so it is in a static state. A significant reflected wave (the substantial free surface elevation in front of the vertical wall) is found to be in the form of a turbulent bore. Secondary wave breaking is observed during offshore propagation, supported by the relatively strong TKE and vorticity intensity from the RANS simulation at t= 9.3 s, 10.4 s and 10.9 s. After the reflected waves propagate into the deep water, the dispersion dominates, and free surface fluctuations emerge (t=14.0 s). For all the above stages, the computed results are in good agreement with the measured results.

4.1.2 *Fringing reef with crest*

A similar evolutionary pattern over the fringing reef with crest is observed from experiments for solitary waves with different nonlinearities. Solitary wave shoals on the fore slope and breaks on the reef crest with significant wave height dissipation. Hydraulic jumps form just at the lee side of the reef crest and then develop into turbulent bores, which propagate over the reef flat and impact

impulsively upon the vertical wall. Hydraulic jumps and vortices are prone to form in the vicinity of the reef crest once the incident and reflected waves pass. Fig. 4 (right) shows spatial snapshots of Case 1 (A/h=0.3) during solitary wave propagation over the crested fringing reef. The simulated TKE and vorticity are presented in Fig. 6.

Overall, the OpenFOAM model can simulate most wave evolutionary stages. Numerical results generally agree qualitatively and quantitatively with experimental data. The solitary wave shoals over the fore reef slope and develops into a plunging breaker onto the reef crest with air entrainment at approximately t=6.0 s. At this initial breaking stage, the TKE intensity is relatively weak, but the maximum vorticity is approximately on the order of O(20 s^{-1}). At approximately t=6.1 s, the broken waves begin to travel down the leeward side of the reef crest and generate a supercritical flow disturbing the still water in the lagoon. Both the simulations and laboratory observations indicate the generation of a hydraulic jump immediately off the back reef and the formation of a downstream propagating turbulent bore with substantial air entrapped on the front, as shown at approximately t=6.7 s, 7.0 s and 7.4 s in Fig. 4 (right).

Meanwhile, the TKE with a maximum value of approximately 0.5 m^2/s^2 is mainly located in front of the breaking wave and is transported downward and backward through vorticity. The generated maximum vorticity is approximately on the order of O(20 s^{-1}). It is interesting to note that the hydraulic jump around the back slope of the reef crest continues to release vorticity during this process. The turbulent bore impacts and climbs up the vertical wall with a sharp dissipated TKE and vorticity intensity (t=9.0 s). At the same time, the aforementioned blank region with zero TKE and vorticity is also noted in the water closely adjacent to the ending wall. The plunging breaking of the reflected waves is supported by the generation of TKE and vorticity near the wavefront at t=10.5 s, as well as by laboratory observations. At approximately t=12.4 s, the reflected wave propagates across the reef crest. Over there, the shallow water depth causes wave breaking, accompanied by the generated TKE on the order of O(0.1 m^2/s^2) and vorticity on the order of O(20 s^{-1}). The reflected wave then begins to travel down the fore reef slope, generates the hydraulic jump with strong vorticity intensity and considerable air bubbles mixing underwater (t=14.0 s). Meanwhile, the offshore water fluctuates, and the TKE and vorticity in the lagoon are diminished. Due to the presence of the reef crest, the originally offshore-headed wave is reflected to the lagoon. This phenomenon is absent from the case without crest.

4.1.3 *The effect of reef crest on wave propagation*

Fig. 7 shows the maximum free surface elevation before wave reflection from the vertical wall for two fringing reef configurations. The variation trend changes after the installation of the reef crest, especially for stronger incident waves. The shallow water depth on the reef crest induces wave breaking and hydraulic formation and thus, rapid wave height decay in the vicinity of the reef crest. The maximum free surface elevation in the lagoon is almost unchanged, denoting steady or quasi-steady turbulent bore formation. The solitary waves do not break in the same region for fringing reefs without a crest, but wave decay also occurs due to wave disintegration over the steep fore slope. The wave height then increases, and the wave breaks on the rear part of the reef flat. The maximum free surface elevations over the reef flat decreased by approximately 22.52%, 23.69%, 29.86%, 30.42% and 22.65% for the presented cases from the top to the bottom due to the shielding effect of the reef crest. OpenFOAM reasonably predicts the measured data except for marginal mismatch over the reef flat.

4.2 *Time history of free surface elevation and flow velocity*

Fig. 8 compares the numerical and experimental results of the time history of local free surface elevation along the wave flume for Case 1 without and with reef crest. OpenFOAM reproduces most evolutionary stages well in both cases. However, there exist some discrepancies. The maximum wave amplitude is underestimated over the reef flat for Case 1 without reef crest at G26 and overestimated for Case 1 with reef crest at G32. The experimental data from the gauges located on the reef flat show apparent fluctuations after the reflected wave passes. However, the RANS modeling fails to capture the fluctuation details (see G20, G26 and G32 for Case 1 in two reef profiles). Such discrepancies may be mainly caused by the unpredictability of turbulent bores with severe wave breaking and the uncertainty of entrapped air bubbles. On the offshore side of the fringing reef, the tail waves after the leading wave and the reflected wave also deviate from the experimental data for both cases. Part of the reason may be that the incident solitary way signal in OpenFOAM is inconsistent with that generated in the physical experiment.

The time history of the horizontal velocity component between the simulated and experimental results at four ADV locations is compared in Fig. 9. At all sites, OpenFOAM successfully captures the onshore motion of the leading wave and offshore motion of the turbulent bore reflected from the

flume ending wall. During the nonlinear shoaling over the fore reef slope at the location of ADV1, the onshore motion of the leading wave for Case 1 without reef crest is symmetrical. In contrast, after installing the reef crest, a clear reflection from the fore reef slope can be found. On the reef flat, the time series has a sharp increase first and then followed by a mild decrease prior to the arrival of the reflected bores. The most apparent disagreement is seen at ADV2. The RANS model does not reproduce the rapid collapse at round t=7.0-7.7 s in the experiments. By carefully observing the wave profile, TKE and vorticity patterns at t =7.4 s in Fig. 4 (right) and Fig. 6, it can be found that a hydraulic jump forms at the back reef crest, with apparent wave breaking, bubble mixing and vorticity motion. In addition, ADV2 is buried in this region (x=42.07 m). Thus, we believe that the complicated and unpredictable flow motion there is attributed to such a discrepancy.

4.3 *Bore impact pressure and force on the vertical wall*

The abovementioned experimental and numerical results have demonstrated the main characteristics of solitary wave breaking, evolving into turbulent bores and impacting vertical wall. To facilitate the following analysis for wave pressure and loads, this process is simplified and sketched in Fig. 10. In this figure, h_s is defined as the still water depth in the reef flat. h_j is the bore height measured from the SWL (Still Water Level), and h_m is the maximum bore height, which is widely used to derive the empirical formula for wave loads and maximum wave pressure (e.g., Asakura et al., 2002; Ikeno and Tanaka, 2003; Mokhtar et al., 2019). v_j is the bore velocity, and h_r is the runup measured from h_j. In the present study. Gauge G32 is used to capture the incident bore height. Fig. 11 depicts the variation in the maximum bore height with respect to the dimensionless incident wave height. The maximum bore height increases with increasing incident wave amplitude for cases with and without a reef crest. The existence of a reef crest reduces the maximum bore height on the reef flat.

Fig. 12 characterizes four numerical stages when the bore arrives at (a) and impacts (b) the vertical wall, then collapses (c) and propagates away (d) from the wall. In the first stage, the turbulent bore splits as liquid flight toward the vertical wall at a high speed (t=8.55 s without reef crest, t=8.67 s with reef crest), causing a great runup with a large amount of air mass mixed (t=8.70 s without a reef crest, t=8.89 s with a reef crest). This very short-duration but severe impact causes the pressure sensor to measure the first peak. After reaching the maximum runup, the water collapses

into the incoming flow and rises to the local water surface, which coincides with the second pressure peak. Vertical downward flow is observed during this stage. Finally, the water is reflected by the vertical wall and propagates offshore.

Figs. 13 and 14 show the comparison of time histories of pressure between experimental data and numerical results for Case 1 without and with a reef crest, respectively. The overall pattern of the impact process is similar for the two reef profile configurations. Each time series has two pressure peaks. The pressure sensors below (P1 to P4) and closely adjacent (P5) to the SWL record a rapid increase to the first peak, which corresponds to the incident bore being redirected up the face of the wall. The pressure then increases more slowly until reaching the second peak, when the runup collapses onto the incoming flow. The peak pressure is followed by a decrease to sustained residual load in a fluctuating way. A reflective bore has now formed and travels offshore. These phenomena agree well with the previous study of Robertson et al. (2013). Above the SWL, i.e., P6–P9 for the reef profile with the absence of a reef crest, the pressure sensors record a pronounced impulsive pressure (an extremely steep front with a considerable peak value) at the initial impact stage. These spikes, however, are not observed in the experiments of Robertson et al. (2013). After that, the runup decreases, and the second peak appears, decreasing to zero after the water body propagates away from the vertical wall. The installation of a reef crest seems to reduce the probability of impulsive impact; in fact, only P6 records the impulsive pressure event.

The numerical model captures the trend of the pressure time series well, but the spike magnitudes are greatly underestimated for the sensors located above the SWL. For Case 1 without and with a reef crest, the maximum errors are approximately 55% (P8) and 47% (P6), respectively. In this region severe splash up and random air entrapment dominate the impact stage, resulting a very complicated flow pattern (as shown in Fig.12) rather difficult to reproduce with OpenFOAM. The measured peak pressure at the sensors of particular interest (P6-P9) is further compared with OpenFOAM simulation in Fig.15. It is not surprising to see that OpenFOAM underestimates the peak pressure for almost all cases with a maximum error of about 50% due to the same reason. To avoid the possible error induced by using large mesh ratio in wave breaking region (Jacobsen et al., 2012), the simulated time series of pressure using Δx=0.0025m and Δz=0.002 m (approximately 1:1 ratio) on reef flat are given in Fig.16. No improvement could be found. Recent OpenFOAM simulations (e.g., Hu et al., 2017; Mitsui et al., 2021) also reported the underestimation of peak

pressure of impulsive wave impact upon structures. The total force time histories on the wall specimen for all cases are obtained by integrating available pressure sensors (e.g., Robertson et al., 2013; Xu et al., 2021) and presented in Fig. 17. The temporal variation trend of the lateral force also follows the two peak patterns. The initial slamming action of the incoming bore causes the first peak. The second peak occurs during the falling action of the water body, which also corresponds to the moment of the maximum force. The maximum force decreases with decreasing incident wave height. The shielding effect of the reef crest on the wave loads on the wall is observed, as listed in Table 2. The peak load is reduced by an average of 20.0%, and the maximum reduction is found for Case 9, which is 30.9%. OpenFOAM successfully captured the loading process of bore impact, runup and reflection from the vertical wall, especially for situations where there is no reef crest. However, the first peak load is slightly overestimated by the model when a reef crest exists.

The vertical pressure distribution along the wall at the peak load is also given in Fig. 18. The linear regression lines fit the experimental data well for the sensors above the SWL. The underwater pressure remains constant. The OCADI (Overseas Coastal Area Development Institute) of the Ports and Harbors Bureau of Japan (2009) documents a similar distribution: a triangular pressure distribution above the SWL and a constant base pressure through the depth of still water h_s. It is noted here that the measurements from Robertson et al. (2013) indicate a uniform linear distribution along the entire water depth. From the figure, we can also see that the underwater pressure increases with increasing incident wave height and is weakened after installing a reef crest.

4.4 *Capability of two existing maximum force estimation equations*

Since the 1980s, many formulas have been proposed in the literature for evaluating tsunami bore pressure exerted on vertical walls. However, it is still challenging to precisely estimate these loads due to the complexity of the interaction between breaking waves and structures. Two formulas will be briefly presented here for later use.

Asakura et al. (2000) carried out physical experiments on bores impacting a vertical wall on a beach with a composite 1:10 slope and proposed the following equation for calculating the force:

$$F = \frac{1}{2}\rho g(3h_j)^2 \tag{1}$$

OCADI (2009) recommends the prediction of the lateral force per unit width on the wall using the

following equation:

$$F = 3.3\rho g h_j^2 + 2.2\rho g h_j h_s \qquad (2)$$

Robertson et al. (2013) proposed a predictive equation based on v_j, h_s, α_s and Fr_r:

$$F = \frac{1}{2}\rho g(h_j + h_s)^2 + \rho(h_j + \alpha_s h_s)v_j^2 + \rho g Fr_r^2 h_r^2 \qquad (3)$$

in which α_s and Fr_r are tuneable parameters. Following Robertosn et al. (2013), the least square method was used to determine the values of these two parameters (α_s =0 and Fr_r =0.2) to obtain the best agreement with the present measurements.

Fig. 19 shows the predicted maximum force from the OpenFOAM simulation, Asakura et al. (2000) (Eq. (1)), OCADI method (Eq. (2)) and Robertson et al. (2013) (Eq. (3)). The solid line defines the ideal trend on which the points would reside if the computed results are equal to the experimental data. The dashed lines denote the range within 20% error. Asakura et al.'s equation almost underestimates the peak load for all cases, and the predictions are scattered around a -20% error line. The OCADI method overestimates the peak force, especially for instances wherein large incident waves propagate toward the fringing reef without a reef crest. Robertson et al.'s equation presents good predictions after finely tuning the parameters. OpenFOAM underestimates the maximum force for fringing reef profiles without reef crests but overestimates it when reef crests exist. The error of predictions from OpenFOAM, the OCADI approach and Robertson et al.'s equation is limited to 20%.

4.5 *Evaluation of the maximum pressure on the vertical wall*

The maximum force exerted on the vertical wall can be calculated by the OpenFOAM and OCADI methods. However, the maximum pressure at specific sensors is out of prediction (more than 55% error at impact area), which is of significant importance for preventing the coastal structure from severely impulsive loading. We herein evaluate two formulas in the literature for maximum wave pressure drawn from laboratory experiments in the literature using the present experimental results. Asakura et al. (2000) argued that the maximum pressure (P_{max}) distribution on an onshore vertical wall can be evaluated by the following bilinear relationship:

$$\frac{P_{max}}{\rho g h_m} = \max\left(3 - \frac{z'}{h_m}, 5.4 - \frac{4z'}{h_m}\right) \qquad (4)$$

13

where z' is the vertical distance from the ground level. Ikeno and Tanaka (2003) proposed the following formulas to estimate the maximum wave pressure on a vertical wall:

$$\frac{P_{\max}}{\rho g h_m} = 3 - \frac{z}{h_m} \quad (0.5 \leq \frac{z}{h_m} \leq 3)$$

$$\frac{P_{\max}}{\rho g h_m} = 4 - 3\frac{z}{h_m} \quad (0 \leq \frac{z}{h_m} \leq 0.5)$$

$$\frac{P_{\max}}{\rho g h_m} = 4 + 3.6\frac{z}{h_m} \quad (-0.5 \leq \frac{z}{h_m} \leq 0)$$

$$\frac{P_{\max}}{\rho g h_m} = 4 + 3.6\frac{z}{h_m} \quad (-0.5 \leq \frac{z}{h_m} \leq 0)$$

$$(5)$$

in which z is the vertical distance from the still water level. The equations have been used and approved reliably by several researchers in past studies (Kato et al., 2006; Lin et al., 2012; Yang, 2017).

In addition to Eqs. (4) and (5), considering the rapid change in the pressure distribution near the SWL, a new predictive equation is also obtained in the form of the exp function, which relates the measured maximum pressure to the maximum incident bore height as:

$$\frac{P_{\max}}{\rho g h_m} = \exp(a - \frac{z}{h_m}) \quad (0.3 \leq z/h_m \leq 3) \ (a = 1.5)$$

$$\frac{P_{\max}}{\rho g h_m} = 0.7\frac{z}{h_m} - 0.11 \quad (0.1 \leq z/h_m \leq 0.3)$$

$$(6)$$

$$\frac{P_{\max}}{\rho g h_m} = 2.1 \quad (z/h_m < 0.1)$$

h_m in the equation is estimated from the measurements of G32, the nearest wave gauge to the vertical wall. The vertical distribution of dimensionless maximum tsunami bore pressure and the estimated results from the three equations are presented in the left panel of Fig. 20. P_{max} was normalized by $\rho g h_m$, and the height of the pressure sensors was normalized by h_m. From the figure, we can conclude that $P_{max}/\rho g h_m$ was mainly determined by z/h_m for the two fringing reef profiles. The equation of Asakura et al. (2002) largely overpredict the maximum pressure in the impact area, but Eq. (5) underestimates it. Both equations overestimate pressure at $z/h_m > 1$. At the locations submerged or close enough to the SWL, the maximum pressure shows marginal variation and approaches a constant 2.1. Similar results are presented by Ikeno and Tanaka (2003). They suggested a constant value of 2.2. The correlation coefficient of Eqs. (4)–(6) are 0.61, 0.68 and 0.83, denoting Eq. (6) has

better performance for the considered experimental cases. It should be mentioned here that Eq.(6) is expected to overestimate the peak loads since the large bottom roughness of a real fringing reef is not considered.

Note that the constant (*a*) in Eq. (6) can be modified to suit different forecast ranges. Fig. 20 (right) presents error bars and the new predicted equation performance after changing constantly. Experimental data variation is within 20% error of the new equation at the location underwater. Above the still water surface, especially for the impact area, the maximum pressure can be predicted quite correctly within a 40% error of the new equation. We can change the constant to fit the large or small value part. For example, constant switching to 1.1, 1.3, 1.7 and 1.9 is suitable to evaluate the result 40% and 20% less and 20 and 40% more than the average value.

5. Conclusions

This paper studies the propagation of solitary waves over idealized fringing reef profiles and the impact exerted by turbulent bores on vertical walls mounted on reef flats using a series of physical experiments and CFD simulations. The experimental data collected can also provide a good benchmark for validating numerical models.

The present results show that incident solitary waves break on the reef flat/crest and develop into turbulent bores. The bores travel over the reef flat and finally impact the vertical wall with severe splash up and air entrapment. Two peaks are observed in the time histories of pressure and lateral force. The maximum force is always achieved at the second peak, which corresponds to runup collapsing onto the incoming flow. Experimental data and some simulation results present the largely impulsive pressure (the first peak) above the SWL during the initial impact stage. The vertical distribution of pressure at peak load is a linear distribution above the SWL and remains constant below the SWL. The existence of a reef crest changes the turbulent bore generation and the subsequent propagation process. The maximum turbulent bore height on the reef flat and the maximum force exerted on the vertical wall are decreased after installing the reef crest, denoting a shielding effect on the structures located on the reef flat, which has profound implications for tsunami bore hazard mitigation.

OpenFOAM simulations demonstrate that it is a powerful tool for representing the details of wave/turbulent bore hydrodynamics, especially the mean dynamics of TKE and vorticity that are

not available in experiments and other types of simulations. Except for the significant underestimation of the first peak (largely impulsive pressure) above the SWL due to the unpredictable nature of the complicated interaction between the turbulent bore and structure, the model qualitatively and quantitatively reproduce the temporal variation in bore pressure. The total lateral force exerted on the vertical wall is well predicted by OpenFOAM with a maximum error of 20% for all considered cases.

The predictive capability of three existing formulas for peak pressure is evaluated using the experimental data. The equation of Asakura presents the maximum deviation from the measurements. The prediction results using the equation of Robertson et al. (2013) fit the present measure well after tuning the parameter. The OCADI method reasonably estimates the maximum load on the vertical wall with a maximum error of 20%. The new proposed equation has better agreement with the collected data, but further validation is still needed.

The present investigation is limited to solitary wave propagation over a fixed water depth and idealized fringe reef profiles. Future research includes conducting laboratory and numerical experiments for various wave conditions under different scales, even considering the large bottom roughness commonly found on actual fringing reefs.

Reference

Arikawa, T., Ikebe, M., Yamada, F., Shimosako, K., Imamura, F., 2005. Large model test of tsunami force on a revetment and on a land structure. Ann. J. Coast. Eng. JSCE. 52, 746-750.

Asakura, R., Iwase, K., Ikeya, T., Takao, M., Kaneto, T., Fujii, N., Ohmori, M., 2000. An experimental study on wave force acting on different breakwater sections due to tsunami overflows. Proc. Coast. Eng. 47, 911-915.

Asakura, R., Iwase, K., Ikeya, T., Takao, M., Kaneto, T., Fujii, N., Ohmori, M., 2002. The tsunami wave force acting on land structures. Coast. Eng., 1191-1202.

Chuang, W., Chang, K., Kaihatu, J., Cienfuegos, R., Mokrani, C., 2020. Experimental study of force, pressure, and fluid velocity on a simplified coastal building under tsunami bore impact. Natural Hazards 103 (1), 1093-1120.

Cuomo, G., Allsop, W., Bruce, T., Pearson, J., 2010. Breaking wave loads at vertical seawalls and

breakwaters. Coast. Eng. 57 (4), 424-439.

Fang, K., Liu, Z., Zou, Z., 2016. Fully nonlinear modeling wave transformation over fringing reefs using shock-capturing Boussinesq model. Journal of Coastal Research. 32 (1), 164-171.

Ferrario, F., Beck, M.W., Storlazzi, C.D., Micheli, F., Shepard, C.C., Airoldi, L., 2014. The effectiveness of coral reefs for coastal hazard risk reduction and adaptation. Nature Communications. 5 (1), 3794.

Ford, M.R., Kench, P.S., 2016. Spatiotemporal variability of typhoon impacts and relaxation intervals on Jaluit Atoll, Marshall Islands. Geology. 44 (2), 159-162.

Goring, D., 1978. Tsunamis-the propagation of long waves onto a shelf, Ph. D. thesis, California insitute of Technology.

Gelfenbaum, G., Apotsos, A., Stevens, A.W., Jaffe, B., 2011. Effects of fringing reefs on tsunami inundation: American Samoa. Earth-Science Reviews. 107, 12-22.

Hoeke, R.K., McInnes, K.L., Kruger, J.C., McNaught, R.J., Hunter, J.R., Smithers, S.G., 2013. Widespread inundation of pacific islands triggered by distant-source wind-waves. Global and Planetary Change. 108, 128-138.

Hu, Z., Mai, T., Greaves, D., Raby, Alison., 2017. Investigations of offshore breaking wave impacts on a large offshore structure. Journal of Fluids and Structures. 75. 99-116.

Ikeno, M., Mori, N., Tanaka, H., 2001. Experimental study on tsunami force and impulsive force by a drifter under breaking bore like Tsunamis. Coastal Engineering Journal. 48, 846-850.

Ikeno, M., Tanaka, H., 2003. Experimental study on Impulse force of drift body and tsunami running up to land. Ann. J. Coast. Eng. JSCE. 50, 721-725.

Jacobsen, N.G., Fuhrman, D.R., FredsØe, J., 2012. A wave generation toolbox for the open-source CFD library: OpenFoam. International Journal for Numerical Methods in Fluids. 70, 1073-1088.

Kato, F., Inagaki, S., Fukuhama, M., 2006. Wave force on coastal dike due to tsunami. Coast. Eng., 5150-5161.

Kazolea, M., Filippini, A., Ricchiuto, M., Abadie, S., Martin Medina, M., Morichon, D., Journeau, C., Marcer, R., Pons, K., LeRoy, S., Pedreros, R., Rousseau, M., 2019. Wave propagation, breaking, and overtopping on a 2D reef: A comparative evaluation of numerical codes for tsunami modelling. European Journal of Mechanics - B/Fluids. 73, 122-131.

Kihara, N., Kaida, H., 2019. An application of Semi-empirical Physical Model of Tsunami-Bore Pressure on Buildings. Front. Built Environ. 5 (3), 1-15.

Ko, H.T.S., Yeh, H., 2018. On the splash-up of tsunami bore impact. Coast. Eng. 131, 1-11.

Lashley, C.H., Roelvink, D., van Dongeren, A., Buckley, M.L., Lowe, R.J., 2018. Nonhydrostatic and surfbeat model predictions of extreme wave runup in fringing reef environments. Coast. Eng. 137, 11-27.

Lee, T.T., Black, K.P., 1978. The energy spectra of surf waves on a coral reef, Proc. Coast. Eng. 1(16), 588-608.

Li, J., Zang, J., Liu, S., 2019. Numerical investigation of wave propagation and transformation over a submerged reef. Coastal Engineering Journal. 61, 1-17.

Lim, H.J., Chang, K.-A., Huang, Z.C., Na, B., 2015. Experimental study on plunging breaking waves in deep water. J. Geophys. Res. Oceans. 120, 2007-2049.

Lin, T., Hwang, K., Hsiao, S., Yang, R., 2012. An experimental observation of a solitary wave Impingement, runup and overtopping on a seawall. Journal of Hydrodynamics. 24 (1), 76-85.

Liu, W., Liu, Y., Zhao, X., 2019. Numerical study of Bragg reflection of regular water waves over

fringing reefs based on a Boussinesq model. Ocean Eng. 190, 106415.

Liu, W., Ning, Y., Shi, F., Sun, Z., 2020. A 2DH fully dispersive and weakly nonlinear Boussinesq-type model based on a finite-volume and finite-difference TVD-type scheme. Ocean Modelling 147, 101559.

Lowe, R.J., Buckley, M.L., Altomare, C., Rijnsdorp, D.P., Yao, Y., Suzuki, T., Bricker, J.D., 2019. Numerical simulations of surf zone wave dynamics using smoothed particle hydrodynamics. Ocean Modelling. 144, 101481.

Lowe, R.J., Falter, J.L., Bandet, M.D., Pawlak, G., Atkinson, M.J., Monismith, S.G., Koseff, J.R., 2005. Spectral wave dissipation over a barrier reef. Journal of Geophysical Research. 110 (C4), 1-16.

Ma, G., Su, S., Liu, S., Chu, J., 2014. Numerical simulation of infragravity waves in fringing reefs using a shock-capturing non-hydrostatic model. Ocean Engineering. 85, 54-64.

Mokhtar, Z.A., Mohammed, T.A., Yusuf, B., Lau, T.L., 2019. Experimental investigation of tsunami bore impact pressure on a perforated seawall. Applied Ocean Research. 84, 291-301.

Mitsui, J., Kawasaki, K., Kubota, H., Suzuki, K., 2021. Blind-test numerical simulation of tsunami wave pressure acting on a land structure. Journal of Disaster Research. 16(7),1005-1014.

Nwogu, O., Demirbilek, Z., 2010. Infragravity wave motions and runup over shallow fringing reefs. Journal of Waterway, Port, Coastal, and Ocean Engineering. 136 (6), 295-305.

Ning, Y., Liu, W.J., Zhao, X.Z., Zhang, Y., Sun, Z.L., 2019. Study of Irregular Wave Run-up over Fringing Reefs based on a Shock-capturing Boussinesq Model, Applied Ocean Research. 86, 216-224.

OCADI, 2009. Technical standards and commentaries for port and harbour facilities in Japan. The Overseas Coastal Area Development Institute of Japan, Ports and Harbours Bureau, Tokyo, Japan.

Quataert, E., Storlazzi, C., van Rooijen, A., Cheriton, O., van Dongeren, A., 2015. The influence of coral reefs and climate change on wave-driven flooding of tropical coastlines. Geophysical Research Letters. 42 (15), 6407-6415.

Robertson, I.N., Paczkowski, K., Riggs, H.R., Mohamed, A., 2013. Experimental investigation of tsunami bore forces on vertical walls. Journal of Offshore Mechanics and Arctic Engineering. 135 (2), 021601.

Roeber, V., Bricker, J.D., 2015. Destructive tsunami-like wave generated by surf beat over a coral reef during Typhoon Haiyan. Nature Communications. 6, 7854.

Roeber, V., Cheung, K.F., 2012. Boussinesq-type model for energetic breaking waves in fringing reef environments. Coast. Eng. 70, 1-20.

Roeber, V., Cheung, K.F., Kobayashi, M.H., 2010. Shock-capturing Boussinesq-type model for nearshore wave processes. Coast. Eng. 57 (4), 407-423.

Storlazzi, C.D., Gingerich, S.B., van Dongeren, A., Cheriton, O.M., Swarzenski, P.W., Quataert, E., Voss, C.I., Field, D.W., Annamalai, H., Piniak, G.A., McCall, R., 2018. Most atolls will be uninhabitable by the mid-21st century because of sea-level rise exacerbating wave-driven flooding. Advanced Science. 4 (4), 9741.

Shao, K.Q., Liu, W.J., Gao, Y.Y., Ning, Y., 2019. The influence of climate change on tsunami-like solitary wave inundation over fringing reefs. Journal of Integrative Environmental Sciences. 16(1), 71-88.

Wen, H., Ren, B., Zhang, X., Yu, X., 2019. SPH modeling of wave transformation over a coral reef with seawall. Journal of Waterway, Port, Coastal and Ocean Engineering. 145 (1), 04018026.

Xu, Z., Melville, B., Whittaker, C., Nandasena, N.A.K., Shamseldin, A., 2021. Mitigation of tsunami

bore impact on a vertical wall behind a barrier. Coast. Eng. 164, 103833.

Yang, X., 2017. Study on slamming pressure calculation formula of plunging breaking wave on sloping sea dike. International Journal of Naval Architecture and Ocean Engineering. 9 (4), 439-445.

Yao, Y., Chen, X., Xu, C., Jia, M., Jiang, C. 2020. Modeling solitary wave transformation and run-up over fringing reefs with large bottom roughness. Ocean Engineering, 218, 108208.

Yao, Y., He, F., Tang, Z., Liu, Z., 2018. A study of tsunami-like solitary wave transformation and runup over fringing reefs. Ocean Eng. 149, 142-155.

Yao, Y., He, T., Deng, Z., Chen, L., Guo, H., 2019. Large eddy simulation modeling of tsunami-like solitary wave processes over fringing reefs. Natural Hazards and Earth System Sciences. 19 (6), 1281-1295.

Yao, Y., Liu, Y., Chen, L., Deng, Z., Jiang, C., 2020. Study on the wave-driven current around the surf zone over fringing reefs. Ocean Eng. 198, 106968.

Zhang, L., Karnauskas, K.B., Donnelly, J.P., Emanuel, K., 2017. Response of the North Pacific tropical cyclone climatology to global warming: Application of dynamical downscaling to CMIP5 models. Journal of Climate. 30 (4), 1233-1243.

Zheng, J., Yao, Y., Chen, S., Zhang, Q., 2020. Laboratory study on wave-induced setup and wave-driven current in a 2DH reef-lagoon-channel system. Coast. Eng. 162, 103772.

Zhou, Q., Zhang, J., Li, Y.S., 2016. Parametric investigation of breaking solitary wave over fringing reef based on shock-capturing Boussinesq model. Coastal Engineering Journal. 58(2), 1650007.

Fig. 1 Sketch of flume layout and apparatus location.

Fig. 2 Time series of free surface elevation (top), flow velocity (middle) and pressure (bottom) from three runs for Case 1 without a reef crest.

Fig. 3 Local grid system around the reef edge and grid sensitivity testing results.

Fig. 4 Wave envelope diagram at characteristic times for cases without a reef crest (left) and with a reef crest (right) (dots: measured data; lines: computed results).

Fig. 5 Computed TKE (left) and vorticity (right) for Case 1 without a reef crest.

Fig. 6 Computed TKE (left) and vorticity (right) for Case 1 with a reef crest.

Fig. 7 Comparison of the maximum free surface elevation before wave reflection from the vertical wall between RANS modeling.

Fig. 8 Comparison of time series of free surface elevation.

Fig. 9 Comparison of time series of flow velocity

Fig. 10 Sketch of tsunami bores impacting a vertical wall.

Fig. 11 Experimental maximum bore height at G32 versus dimensionless incident wave height.

Fig. 12. Contour maps of the water volume fraction and vector illustrations of the velocity (arrows) at the stages of the impact for Case 1 without a reef crest (top) and with a reef crest (bottom) ((a) turbulent bore arrives at the vertical wall; (b) bores are redirected up (the first peak); (c) the collision of falling down water body with incoming flow; (d) reflected wave propagate away from the vertical wall).

Fig. 13 Comparison of time series of dynamic pressure between measurements from three runs (dashed lines) and computed results (solid line) for Case 1 without a reef crest.

Fig. 14 Comparison of time series of dynamic pressure between measurements (dashed lines) and computed results (solid line) for Case 1 with a reef crest.

Fig. 15 Predicted peak pressure versus experimental data in the impact area (dashed line denotes 50% deviation).

Fig. 16 Comparison of time series of dynamic pressure simulated with different mesh size for Case 1 without reef crest (dashed lines: $\Delta x=0.0025m$, $\Delta z=0.002$ m; solid line: $\Delta x=0.005m$, $\Delta z=0.002$ m).

Fig. 17 Comparison of time histories of lateral force during turbulent bore impact of the vertical wall for cases without a reef crest (top) and with a reef crest (bottom) (black solid lines: computed results; dashed lines: experimental data from three runs).

Fig. 18 Measured dynamic pressure distribution on the wall at peak load for cases without a reef crest (top) and with a reef crest (bottom) (solid lines: linear fit; scattered dots: data).

Fig. 19 Predicted maximum force versus experimental maximum force.

Fig. 20 Vertical distribution of dimensionless maximum tsunami bore pressure and validation by predicted equations (left) and the new equation performance with varying values of *a* in Eq. (6) (right).
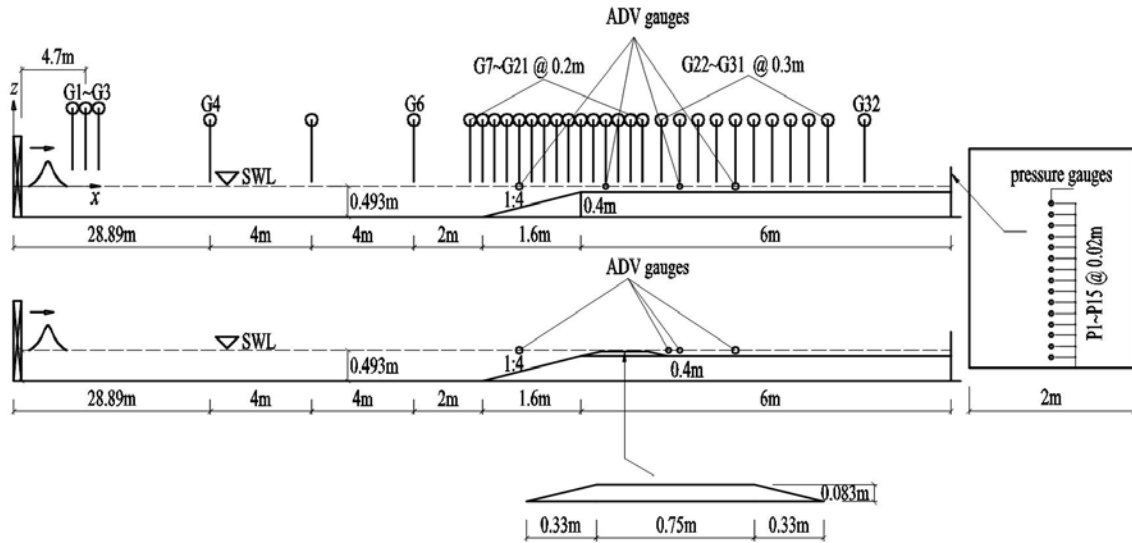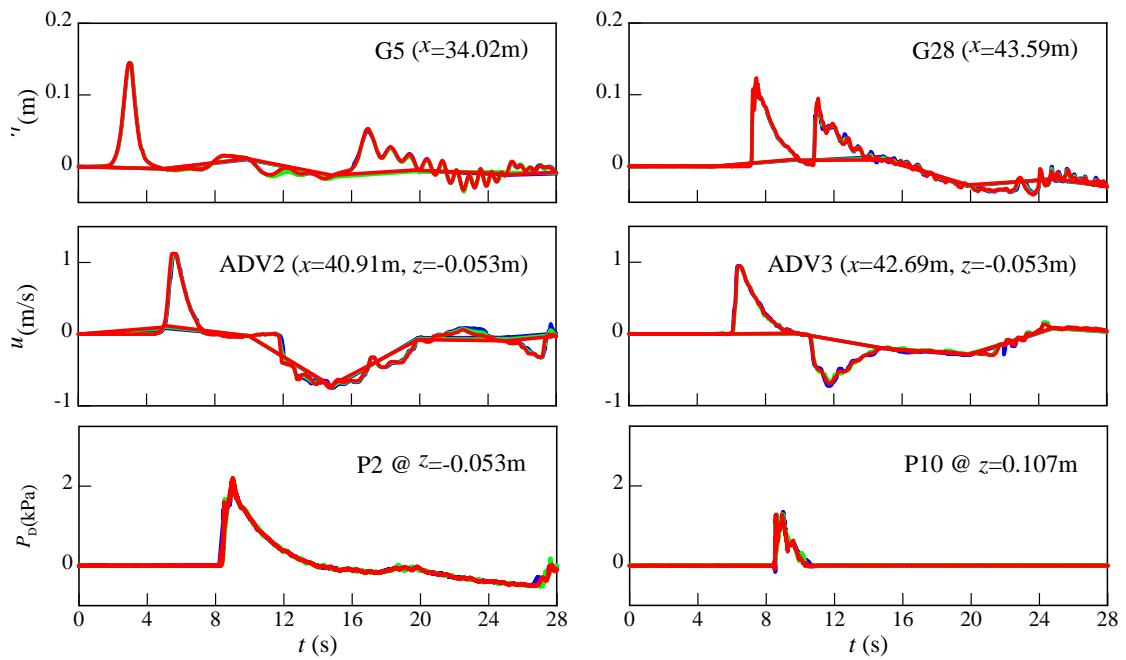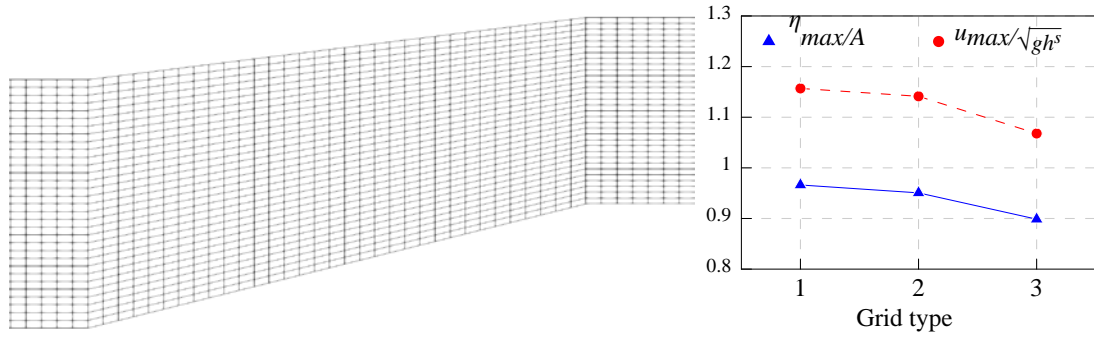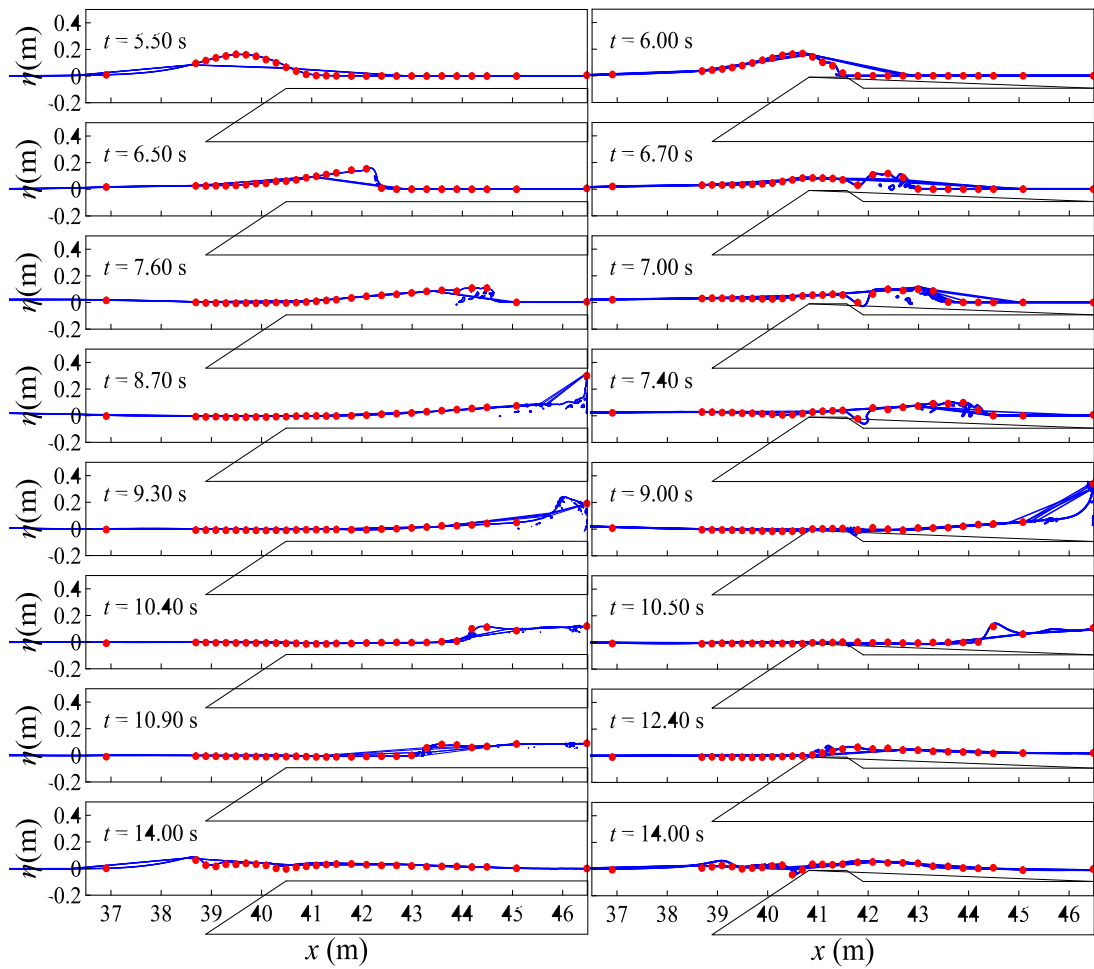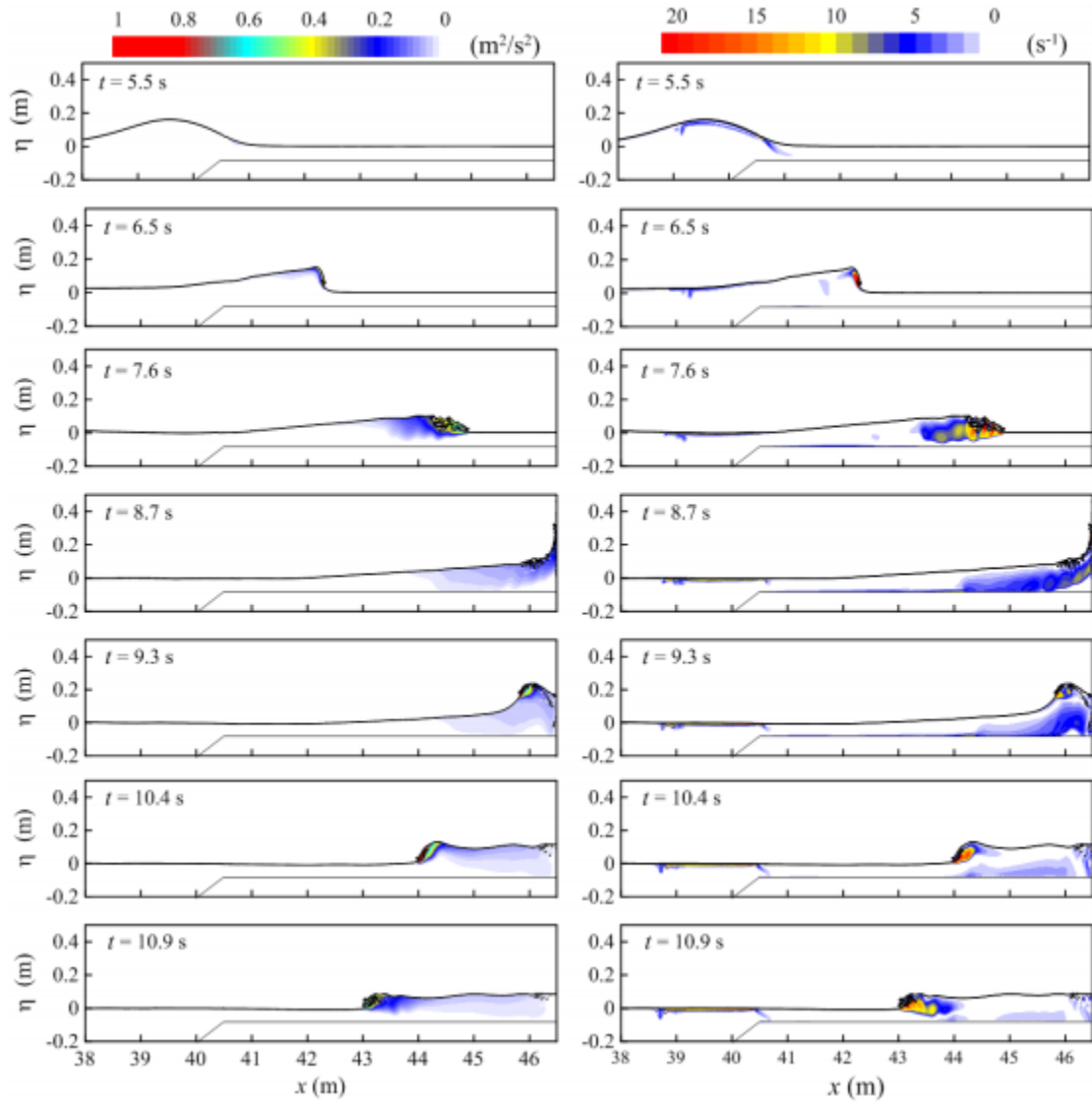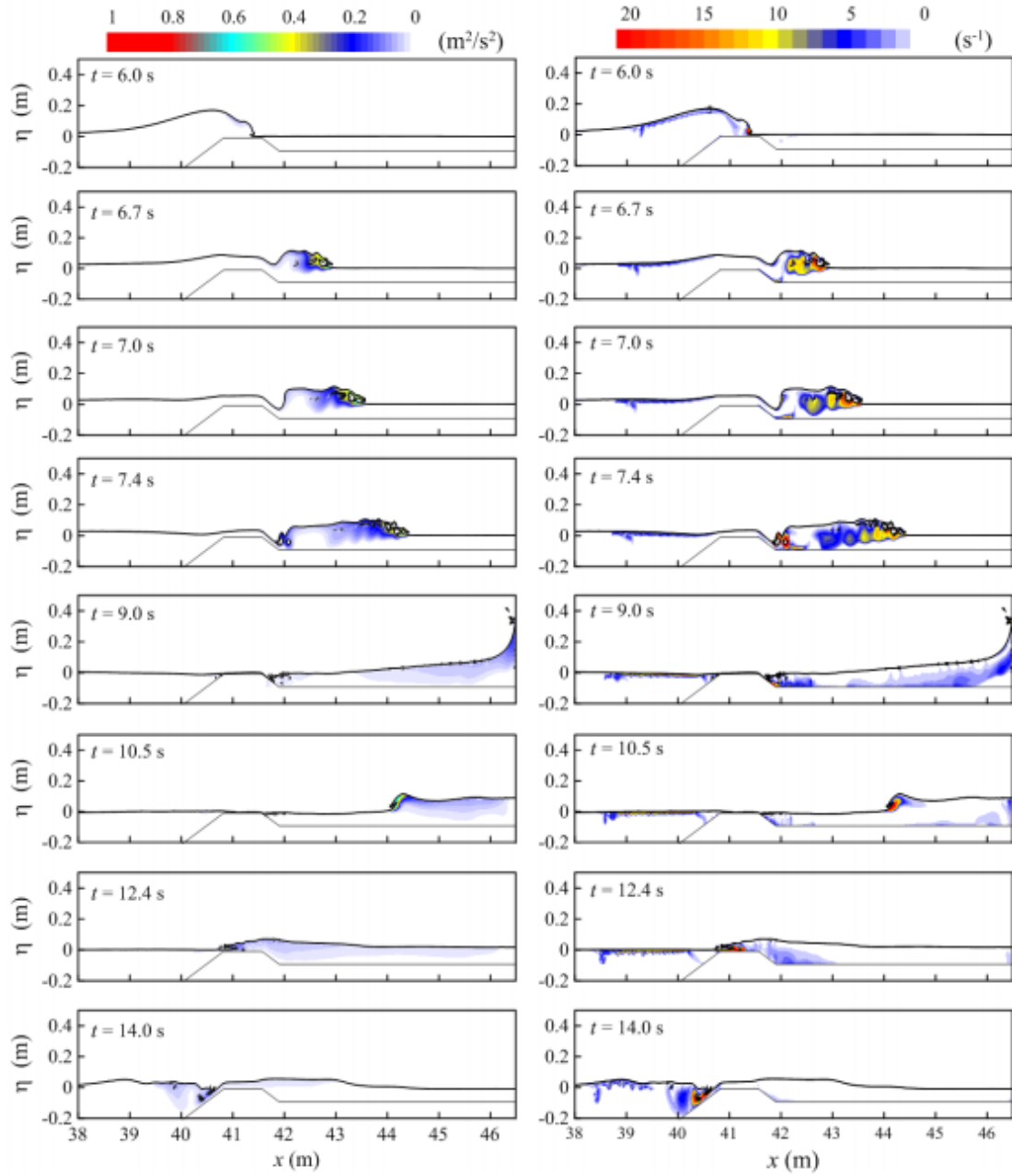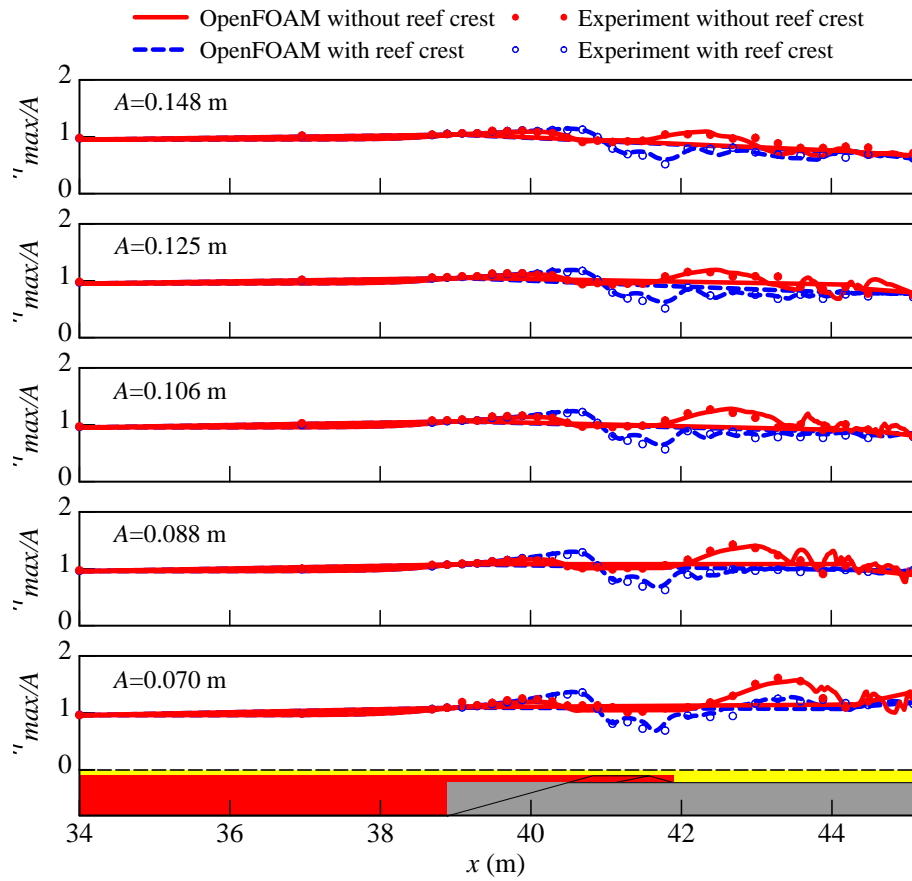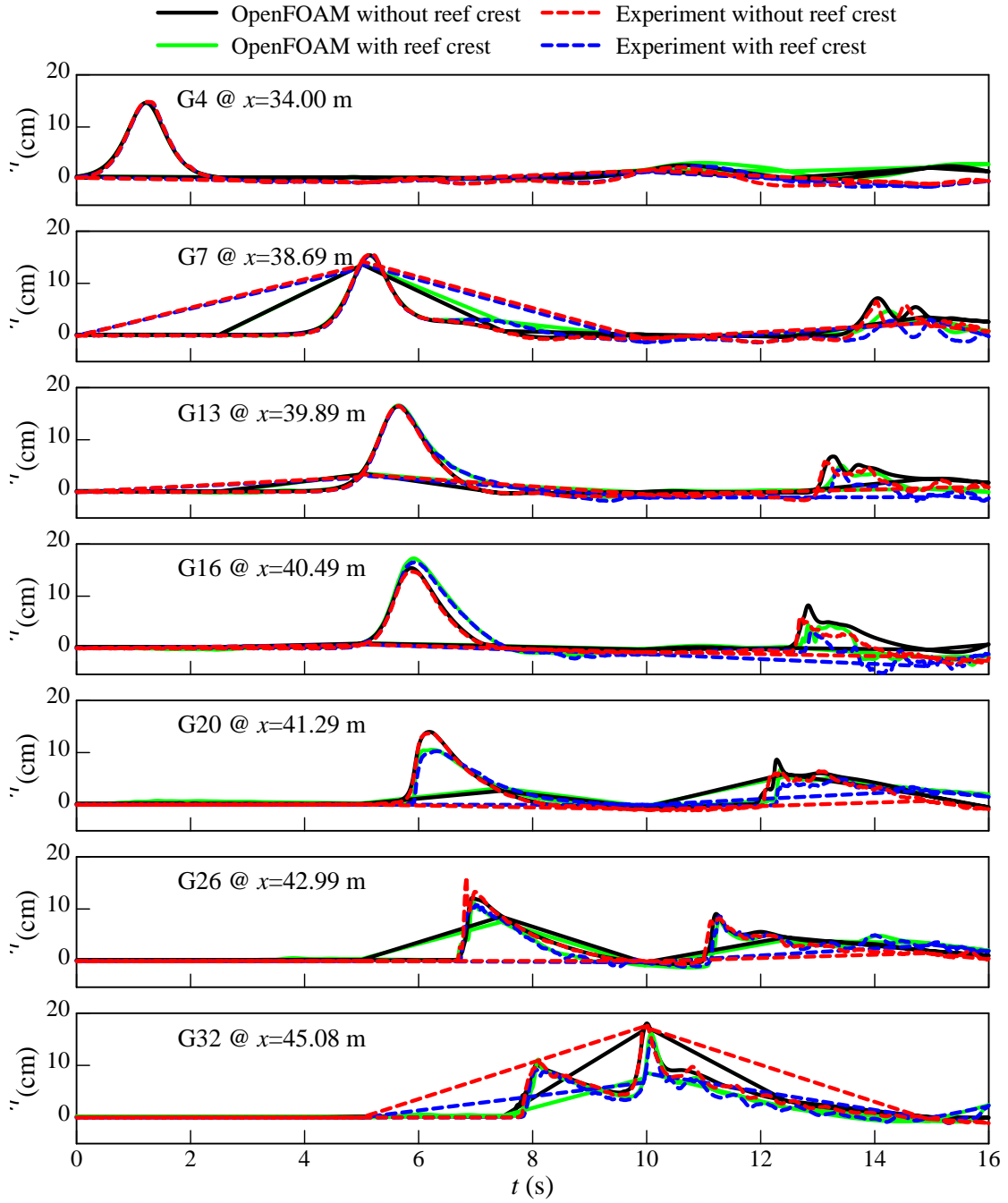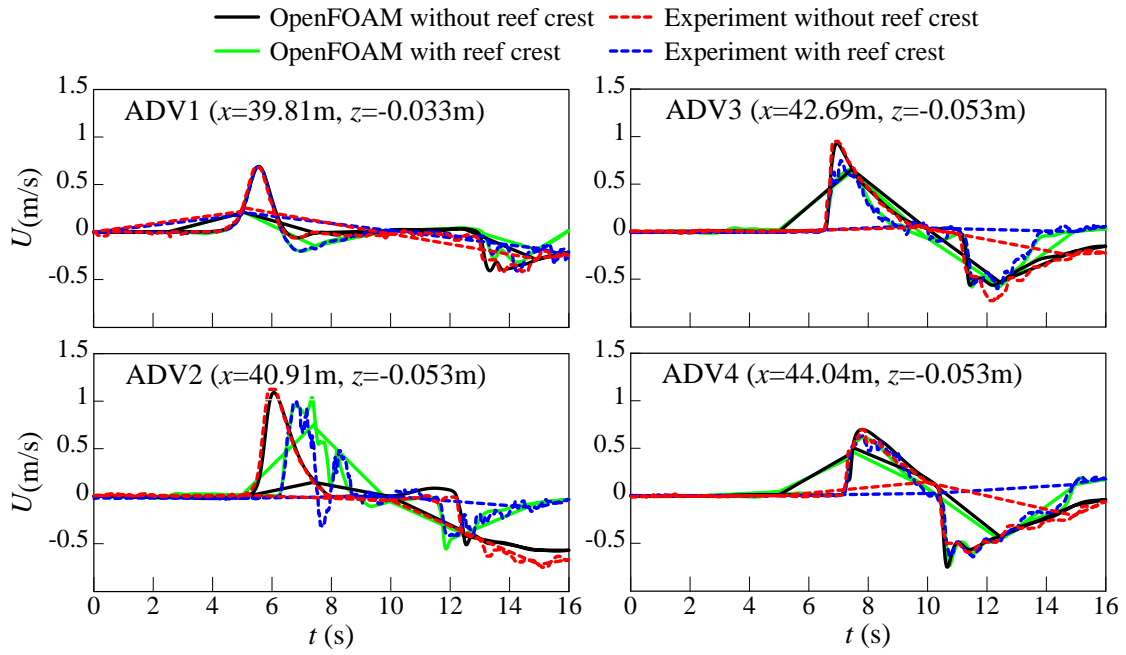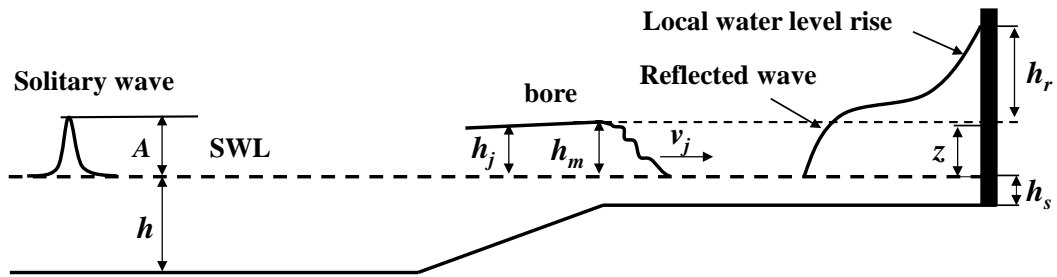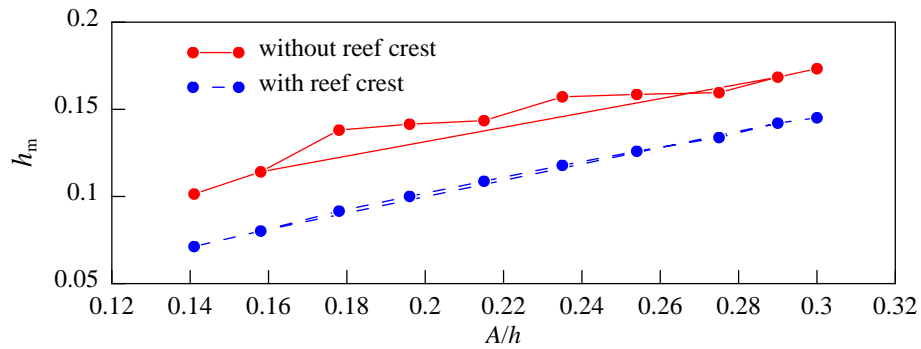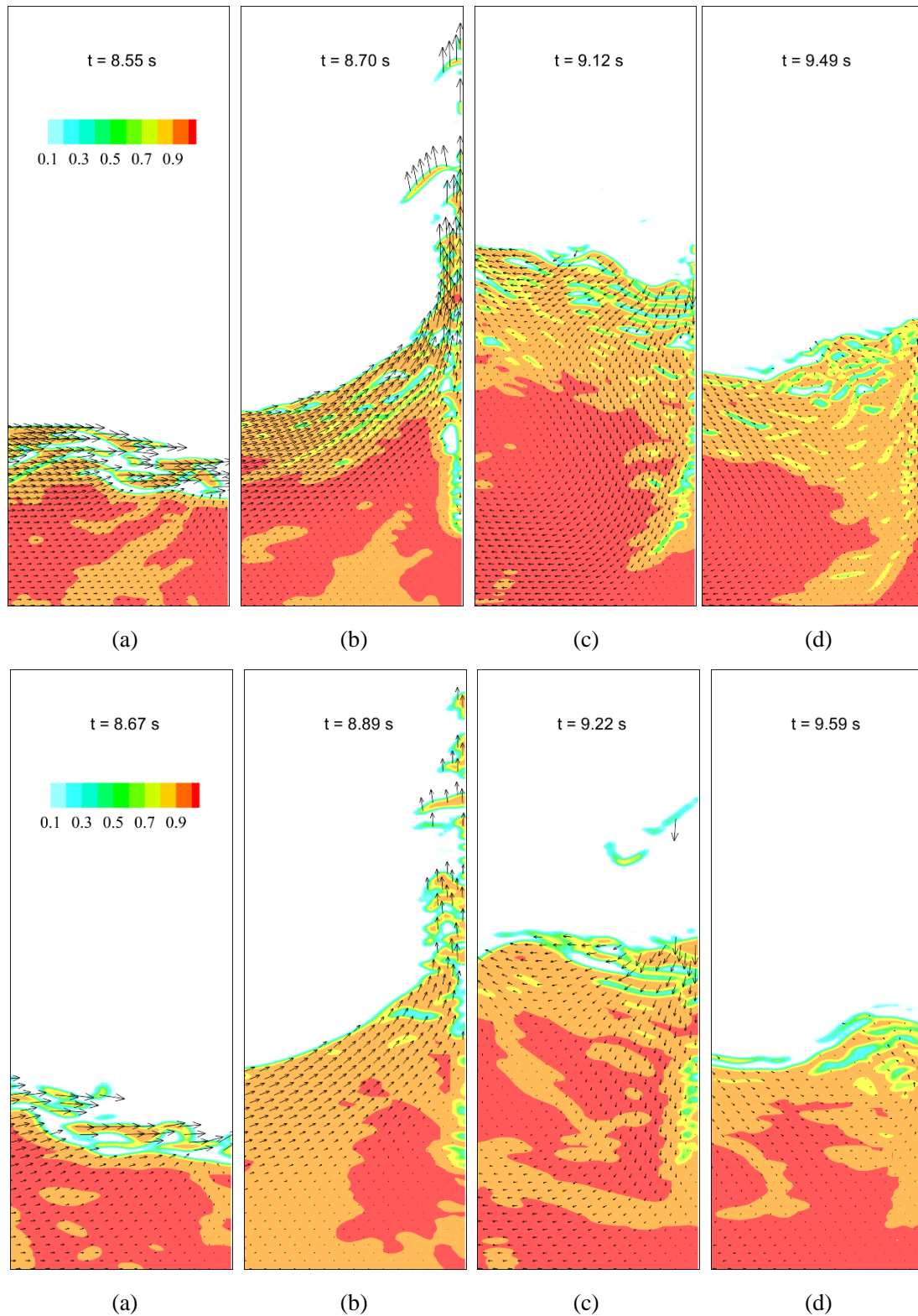
Fig. 1 Sketch of flume layout and apparatus location.

Fig. 2 Time series of free surface elevation (top), flow velocity (middle) and pressure (bottom) from three runs for Case 1 without a reef crest.

Fig. 3 Local grid system around the reef edge and grid sensitivity testing results.

Fig. 4 Wave envelope diagram at characteristic times for cases without a reef crest (left) and with a reef crest (right) (dots: measured data; lines: computed results).

Fig. 5 Computed TKE (left) and vorticity (right) for Case 1 without a reef crest.

Fig. 6 Computed TKE (left) and vorticity (right) for Case 1 with a reef crest.

Fig. 7 Comparison of the maximum free surface elevation before wave reflection from the vertical wall between RANS modeling.

Fig. 8 Comparison of time series of free surface elevation.

Fig. 9 Comparison of time series of flow velocity.

Fig. 10 Sketch of tsunami bores impacting a vertical wall.

Fig. 11 Experimental maximum bore height at G32 versus dimensionless incident wave height.

Fig. 12 Contour maps of the water volume fraction and vector illustrations of the velocity (arrows) at the stages of the impact for Case 1 without a reef crest (top) and with a reef crest (bottom) ((a) turbulent bore arrives at the vertical wall; (b) bores are redirected up (the first peak); (c) the collision of falling down water body with incoming flow; (d) reflected wave propagate away from the vertical wall).

Fig. 13 Comparison of time series of dynamic pressure between measurements from three runs (dashed lines) and computed results (solid line) for Case 1 without a reef crest.

Fig. 14 Comparison of time series of dynamic pressure between measurements (dashed lines) and computed results (solid line) for Case 1 with a reef crest.
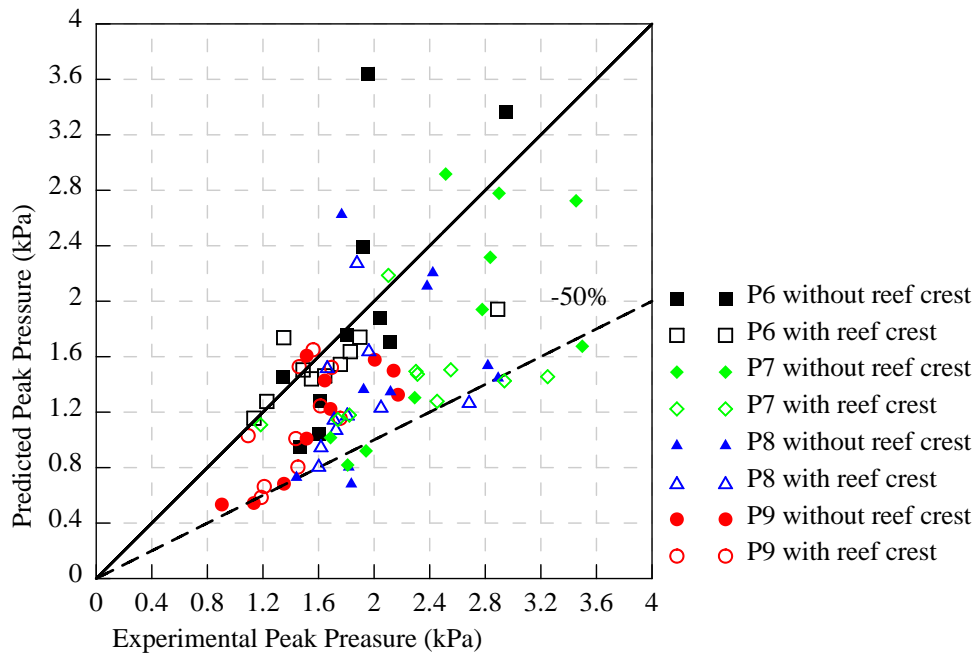
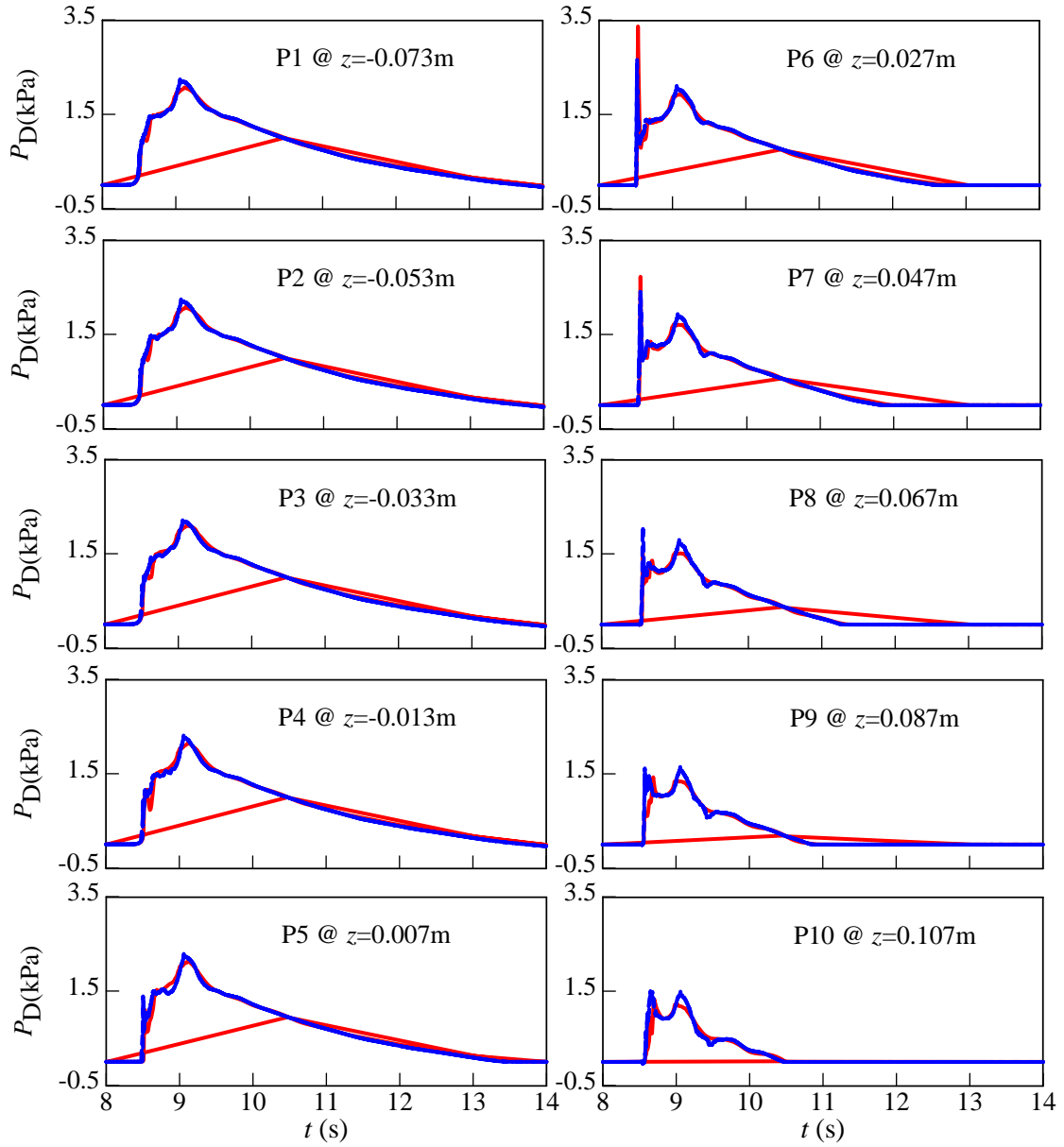**Fig. 15** Predicted peak pressure versus experimental data in the impact area (dashed line denotes 50% deviation).

Fig. 16 Comparison of time series of dynamic pressure simulated with different mesh size for Case 1 without reef crest (dashed lines: Δx=0.0025m, Δz=0.002 m; solid line: Δx=0.005m, Δz=0.002 m).
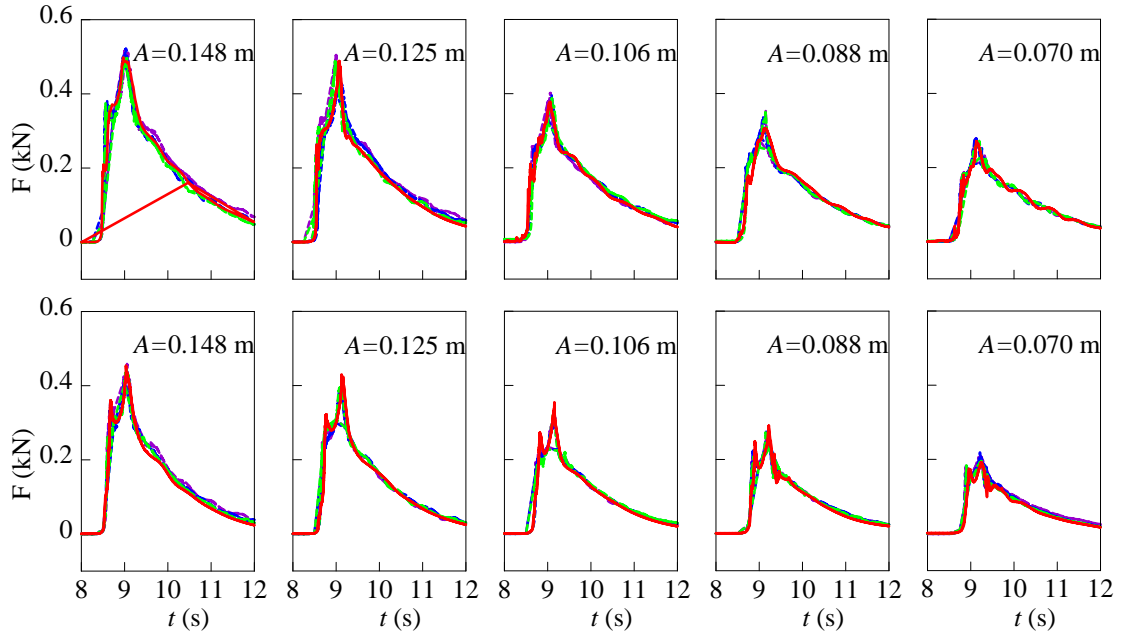
Fig. 17. Comparison of time histories of lateral force during turbulent bores impact of the vertical wall for cases without a reef crest (top) and with a reef crest (bottom) (black solid lines: computed results; dashed lines: experimental data from three runs).
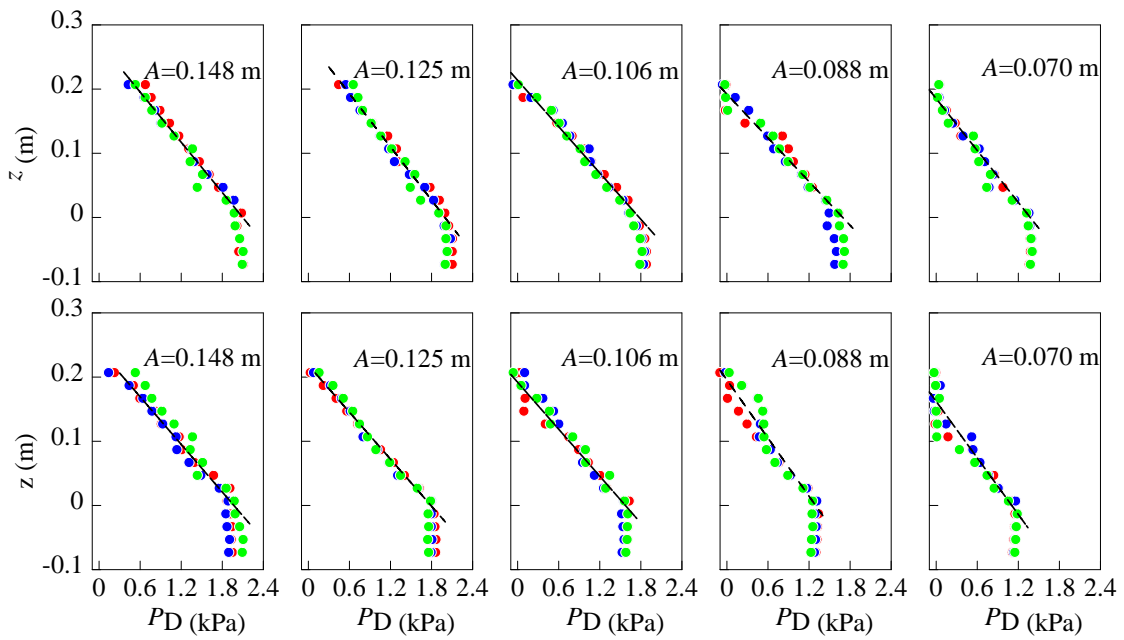

Fig. 18 Measured dynamic pressure distribution on the wall at peak load for cases without a reef crest (top) and with a reef crest (bottom) (solid lines: linear fit; scattered dots: data).
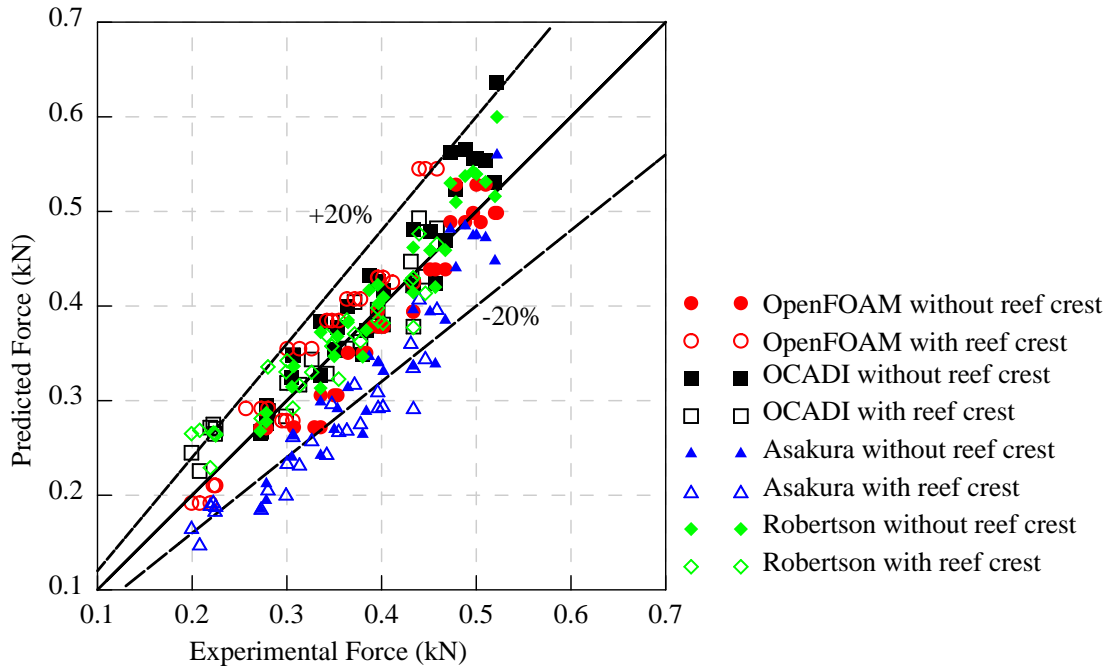
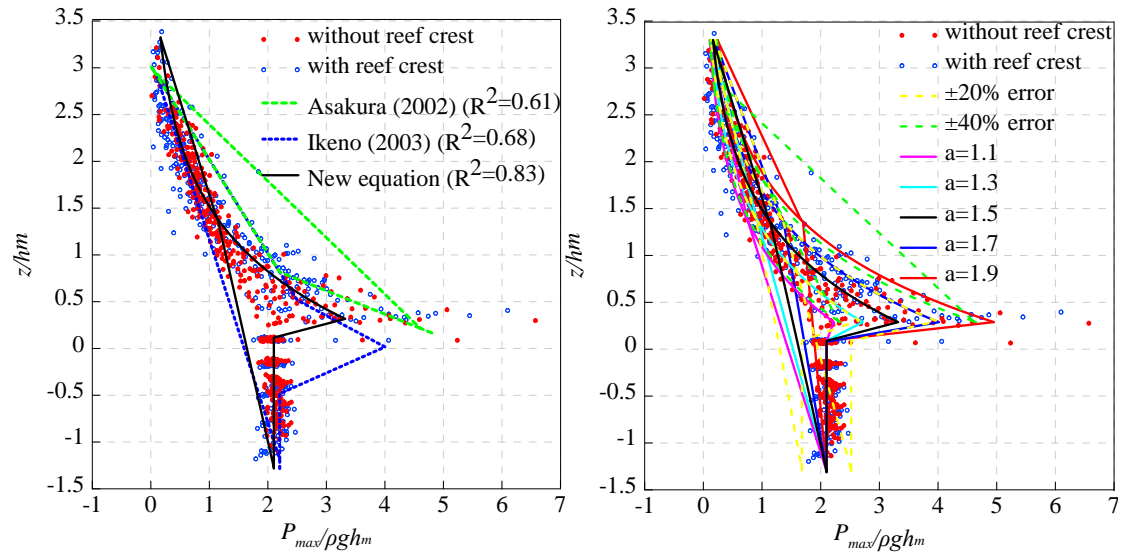**Fig. 19** Predicted maximum force versus experimental maximum force.

Fig. 20 Vertical distribution of dimensionless maximum tsunami bore pressure and validation by predicted equations (left) and the new equation performance with varying values of *a* in Eq. (6) (right).

Table 1 Solitary wave conditions in the experiments.

Case	1	2	3	4	5	6	7	8	9	10
A(m)	0.148	0.143	0.135	0.125	0.116	0.106	0.097	0.088	0.078	0.070
Ratio(A/h)	0.300	0.290	0.275	0.254	0.235	0.215	0.196	0.178	0.158	0.141

Table 2 A summary of peak load exerted on the vertical wall (kPa).

Case	1	2	3	4	5	6	7	8	9	10
Without reef crest	0.513	0.496	0.488	0.458	0.421	0.395	0.376	0.346	0.324	0.276
With reef crest	0.448	0.426	0.398	0.371	0.348	0.313	0.300	0.270	0.224	0.209
Reduced by(%)	12.6	14.1	18.4	19.1	17.3	20.7	20.2	22.1	30.9	24.4